ADVANCED OPTICAL MATERIALS
www.advopticalmat.de

Boosting Reverse Intersystem Crossing of TADF Emitter through Molecular Geometry Adaptation to Crystalline Host

*Gediminas Kreiza, Tomas Javorskis, Edvinas Orentas, and Karolis Kazlauskas**

Rapid reverse intersystem crossing (RISC) is one of the prime concerns for blue thermally activated delayed fluorescence (TADF) emitters, as it reduces triplet exciton population, the root cause of detrimental triplet-mediated annihilation processes that accelerate device efficiency roll-off and degradation. This work introduces a new concept to tailor the RISC of TADF emitters through their molecular geometry adaptation to crystalline hosts bearing a similar donor-acceptor structure. A meticulously designed crystalline host comprising isophthalonitrile acceptor (A) and carbazole-derived donor (D) units, characterized by nearly orthogonal D-A arrangement, has been demonstrated to alleviate singlet-triplet energy gap (ΔE_{ST}) of the TADF dopant by forcing it to adopt a more twisted D-A configuration, as corroborated by X-ray diffraction (XRD) measurements. The approach not only significantly reduces the RISC activation energy, resulting in a remarkable tenfold boost of the RISC rate (above 10^7 s^{-1}) and fourfold shortening of delayed FL lifetime (down to 1.5 µs), but also offers the additional benefit of suppressing conformational disorder of TADF dopant, producing a narrower emission bandwidth. The presented concept, based on crystalline host-driven RISC engineering, is anticipated to have a profound impact on the development of high-performance, stable blue-emitting TADF organic light-emitting diodes (OLEDs).

1. Introduction

There is an increasing demand for noble metal-free organic emitters in organic light-emitting diodes (OLEDs) and OLED-based applications, which include large-area, high-resolution displays, and solid-state lighting.[1] While heavy metal-containing phosphorescent emitters offer the potential to attain ≈ 100% internal quantum efficiencies in OLEDs, their usage is hindered by high costs and stability issues in the blue spectral range arising from weak metal-ligand coordination bonds.[2,3] Purely organic and highly efficient 3rd generation emitters, relying on thermally activated delayed fluorescence (TADF) phenomena, have been successfully developed and proposed as a viable alternative to phosphorescent emitters.[4] TADF facilitates the upconversion of "dark" triplet excitons to the singlet manifold through the reverse intersystem crossing (RISC) process, allowing them to be harvested with 100% efficiency. Consequently, TADF-OLEDs with external quantum efficiencies (EQE) exceeding 20% have been realized.[5–7]

Despite their advantages and potential, blue-emitting TADF-OLEDs still face challenges associated with severe efficiency roll-off and poor device stability.[8,9] These challenges are traced back to their high triplet energies as well as the prolonged delayed fluorescence lifetime, which is inherent in the extended triplet exciton lifetime.[10] Triplets that persist on a timescale of a few microseconds and longer can be detrimental to device performance, particularly at higher current densities. This is because they initiate the formation of high-energy excited states via triplet-triplet, triplet-polaron, or triplet-singlet annihilation, ultimately leading to bond scission.[11,12] To reduce the triplet lifetime in blue TADF devices, it is necessary to ramp up the RISC rate (k_{RISC}) while concurrently maintaining high radiative decay rates from the singlet state. Considering that the majority of reported blue TADF compounds exhibit k_{RISC} similar to or below 10^6 s^{-1},[13–15] this underscores the importance of a deeper insight into the TADF process. It also emphasizes the need for further development of molecules with rapid RISC, which is crucial for ensuring stable device operation at high current densities.[6,15] According to Fermi's Golden rule, k_{RISC} can be enhanced through several mechanisms: i) enlarging spin-orbit coupling (SOC) matrix element from T_n to S_1, which implies considering intermediate triplet states and their vibronic coupling with the lowest singlet charge transfer (CT) state; ii) decreasing reorganization energy through the suppression of structural changes upon $T_n \rightarrow S_1$ conversion; iii) minimizing ΔE_{ST} by

G. Kreiza, K. Kazlauskas
Institute of Photonics and Nanotechnology
Vilnius University
Saulėtekio av. 3, Vilnius LT-10257, Lithuania
E-mail: karolis.kazlauskas@ff.vu.lt
T. Javorskis, E. Orentas
Department of Organic Chemistry
Faculty of Chemistry and Geosciences
Vilnius University
Naugarduko 24, Vilnius LT-03225, Lithuania

The ORCID identification number(s) for the author(s) of this article can be found under https://doi.org/10.1002/adom.202400024

DOI: 10.1002/adom.202400024

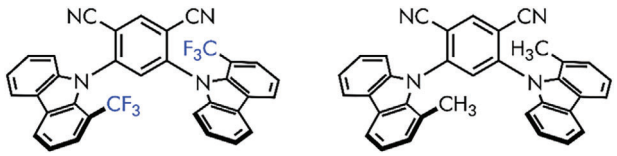

Figure 1. Chemical structures of the investigated IPN compounds.

reducing HOMO-LUMO overlap in donor-acceptor (D-A) compounds with pronounced charge transfer (CT) character.[16] Following these principles, successful tailoring of the RISC rate has been achieved mainly through molecular engineering or by adjusting guest-host interactions.[17–21] For instance, the introduction of functional/steric groups has been demonstrated to induce CT-LE triplet state mixing[13,22] or cause more twisted configurations with reduced ΔE_{ST}.[15,23] On the other hand, choosing the proper host polarity was shown to aid in aligning singlet and triplet manifolds in TADF guest, thereby also reducing the energetic barrier for RISC.[24,25] Notably, no attempts have been made yet to manipulate the RISC process by doping TADF emitter into the crystalline host with the intent to adopt the structural configuration of pre-twisted host molecules. This concept is intriguing, not only from the fundamental perspective but also from a practical standpoint, as crystalline OLEDs would offer superior morphological stability, coupled with the ability to withstand higher current densities.[26,27]

To this end, we designed and investigated a guest-host system comprising the previously reported efficient blue TADF emitter 4,6-bis(1-methylcarbazol-9-yl)benzene-1,3-dicarbonitrile (DMeCz-IPN) as a guest, doped into a crystalline host 4,6-bis[1-(trifluoromethyl)carbazol-9-yl]benzene-1,3-dicarbonitrile (DCF3Cz-IPN). The host, with a molecular structure identical to the dopant except for the inclusion of more sterically demanding trifluoromethyl (-CF3) groups, exhibited a more twisted geometry. The realization of doped crystals has been found to infer changes in the geometry of the dopant, aligning it with the pre-twisted structural configuration of the host. The alignment led to an impressive almost tenfold boost in the RISC rate, reaching up to 1.32×10^7 s^{-1}, along with a substantial fourfold reduction in delayed fluorescence lifetime, down to 1.52 µs.

2. Results and Discussion

The compounds examined in this study shared the same molecular backbone, consisting of an isophthalonitrile (IPN) acceptor singly bonded with two meta-linked carbazole (Cz) donor units. The sole distinction in the structures of these compounds was the introduction of different substituents in the first position of the carbazoles. Specifically, the compound DMeCz-IPN featured methyl groups, while DCF3Cz-IPN incorporated trifluoromethyl (-CF_3) moieties (see **Figure 1**). The synthesis of DMeCz-IPN was described previously,[23] and DCF3Cz-IPN was synthesized in an analogous fashion using the corresponding 1-(trifluoromethyl)−9*H*-carbazole obtained via Catellani reaction.[28] The detailed synthesis procedure along with the structural identification data can be found in the Electronic Supplementary Information (ESI).

Quantum chemical calculations revealed that these modifications to the Cz induce essential changes in the geometry of the IPN compounds. In the ground state of DMeCz-IPN, the methyl-substituted Cz donors form a 70° angle with the IPN acceptor. In contrast, in the case of DCF3Cz-IPN, the substitution imposes greater D-A twisting, with an angle of 86°, due to the sterically more demanding CF_3 moieties. The analysis of molecular orbitals (see Figure S4, Supporting Information) showed that both compounds exhibit a strong CT character, with the HOMO localized on Cz and the LUMO on the IPN unit. As anticipated, the larger D-A twist angle in DCF3Cz-IPN resulted in significantly weaker oscillator strengths (*f*) for the ground-to-excited state transition energies compared to those of DMeCz-IPN (Table S1, Supporting Information). However, despite the larger twisting, DCF3Cz-IPN exhibited a higher $S_0 \rightarrow S_1$ transition energy (3.41 eV) than DMeCz-IPN (3.27 eV), as determined from time-dependent density-functional theory (TD-DFT) calculations. This finding emphasizes the dual role of $-CF_3$ groups: they impact the molecular geometry and, at the same time, reduce the electron-donating properties of Cz donors, leading to an expected emission at shorter wavelengths compared to DMeCz-IPN.

The absorption spectra of the IPN compounds in toluene (**Figure 2**) correlated well with the results of DFT calculations. DMeCzIPN displayed a broad, unstructured CT absorption band that peaked at 383 nm. In contrast, the absorption of DCF3Cz-IPN was of lower intensity and shifted to shorter wavelengths (356 nm). The lower intensity of the CT band in DCF3Cz-IPN corresponded with the weaker *f* obtained from DFT. Meanwhile, structured higher-intensity absorption bands at 330 and 318 nm, which are characteristic of both compounds, were assigned to LE transitions typical of carbazole.[29]

The emission properties of the IPN compounds were investigated and compared in amorphous DPEPO films at 10 wt.% doping concentration (Figure 2a,b). DMeCz-IPN exhibited broadband fluorescence with a peak at 484 nm, while DCF3Cz-IPN displayed emission peaking at 439 nm. Analyzing the low-temperature (10 K) emission of films allowed the evaluation of ΔE_{ST} values, which were determined to be 50 and 150 meV for DMeCz-IPN and DCF3Cz-IPN, respectively (see Figure S5, Supporting Information). The key photophysical properties of the studied films are summarized in **Table 1**. Fluorescence quantum yields (Φ_{FL}) along with room-temperature fluorescence transients featuring distinct delayed (DF) and prompt (PF) fluorescence components (see Figure 2c) were utilized to calculate the TADF properties of IPNs. DMeCz-IPN demonstrated efficient fluorescence ($\Phi_{FL} = 0.75$) with a relatively fast DF (5.26 µs) due to a high k_{RISC} reaching 1.5×10^6 s^{-1}. Remarkably, Φ_{FL} of DCF3Cz-IPN was reduced to 0.38, and the DF was prolonged to 10.3 µs, with a corresponding k_{RISC} of 0.56×10^6 s^{-1}, which is mainly attributed to a larger ΔE_{ST}. Given that k_{RISC} is approximately one order of magnitude larger than the non-radiative decay rate from the triplet state (k_{nr}^T) for both compounds, RISC emerges as the prime triplet deactivation pathway. Consequently, the lower Φ_{FL} of DCF3Cz-IPN can be attributed to the dominance of ISC over radiative decay, in addition to a sluggish RISC rate.

Despite DCF3Cz-IPN displaying TADF properties that are less effective than those of DMeCz-IPN from an emitter perspective, its shorter-wavelength emission and the energetic compatibility of its HOMO and LUMO levels (refer to Table S2 (Supporting

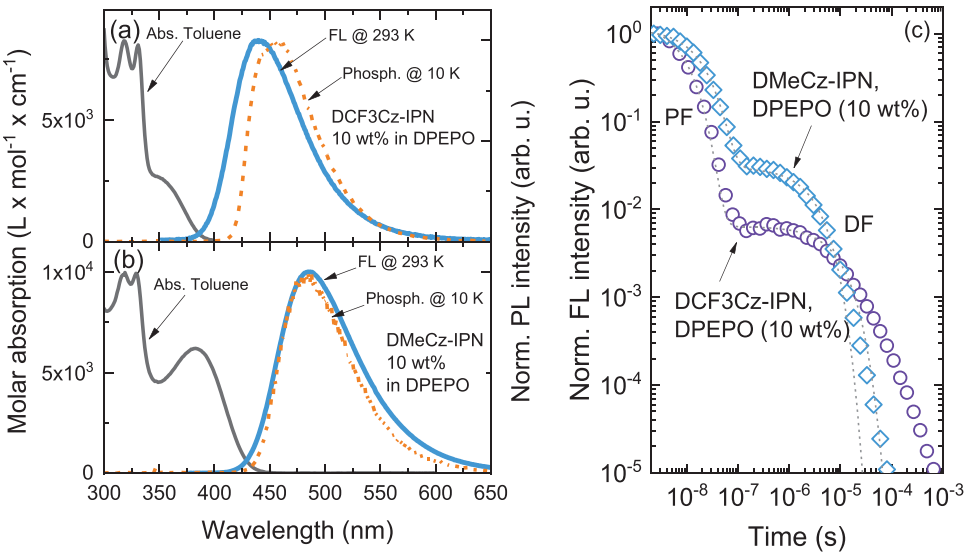

Figure 2. Absorption spectra in dilute toluene solution, room-temperature fluorescence, and low-temperature phosphorescence (100 µs delay) spectra of a) DCF3Cz-IPN and b) DMeCz-IPN in DPEPO at 10 wt.% doping concentration. c) Room-temperature fluorescence transients of IPN compounds in DPEPO at 10 wt.% doping concentration. The dashed lines indicate double-exponential decay fits.

Table 1. Main photophysical properties of the IPN compounds in amorphous DPEPO and crystalline DCF3Cz-IPN matrix at 10 wt.% doping concentration.

IPN compound	Matrix	Φ_{FL} [a)]	Φ_{DF}/Φ_{PF}	τ_{PF} (ns)	τ_{DF} (µs)	k_r (10^6 s^{-1})	k_{RISC} [b)] (10^6 s^{-1})	k_{ISC} [b)] (10^7 s^{-1})	k_{nr}^T [b)] (10^4 s^{-1})	S_1/T_1 [c)] (eV)	ΔE_{ST} (eV)
DCF3Cz-IPN	Amorphous DPEPO	0.38	5.42	9.1	10.3 [d)]	6.47	0.56	10.29	6.4	3.12/2.97	0.15
DMeCz-IPN		0.75	4.79	20.4	5.26 [d)]	6.24	1.50	4.16	5.5	2.87/2.82	0.05
DMeCz-IPN	Crystalline DCF3Cz-IPN	0.78	14.6	20.9	1.52	2.39	13.2	3.29	15.2	2.74/2.72	0.02

[a)] Φ_{FL} was determined in an oxygen-free environment; [b)] k_{ISC}, k_{RISC} and k_{nr}^T were calculated by employing equations reported in Refs;[30,31] [c)] evaluated from the onset of fluorescence and phosphorescence spectra; [d)] average of 3-exponential decay fits of DF component.

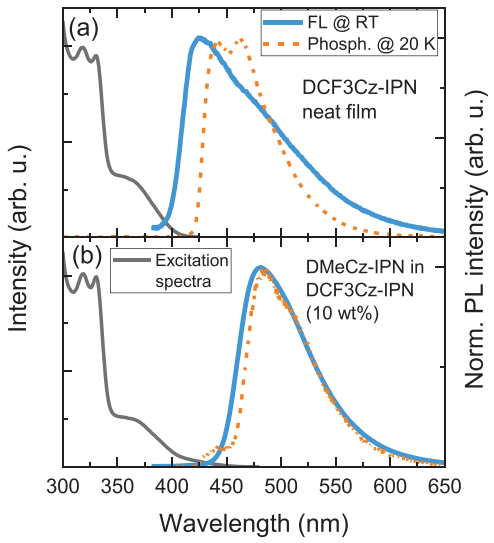

Figure 3. Excitation, room-temperature fluorescence, and phosphorescence (20 K, 100 µs delay) spectra of a) neat and b) 10 wt.% DMeCz-IPN doped DCF3Cz-IPN films.

Information) for cyclic voltammetry data) make DCF3Cz-IPN a suitable candidate for use as a TADF host for DMeCz-IPN.

To evaluate the potential of DCF3Cz-IPN as a host, we initially examined the optical properties of its neat films (**Figure 3**a). At room temperature, the films exhibited fluorescence peaking at 424 nm with a Φ_{FL} of only 0.036 due to concentration quenching. Interestingly, even a slight increase in the doping concentration of DMeCz-IPN (0.5 wt.%) led to a significant increase in Φ_{FL} (see Figure S7, Supporting Information). We found the optimal concentration of DMeCz-IPN to be 10 wt.%, which resulted in a maximum Φ_{FL} of 0.78. This balance was achieved by increasing the Förster resonance energy transfer (FRET) from the host to the dopant at lower concentrations and managing the concentration quenching of the dopant at higher concentrations. The efficient FRET at the doping level of 0.5 wt.% and above is evidenced by the fluorescence signal from the host DCF3Cz-IPN being two orders of magnitude lower than that from the dopant (see Figure S8, Supporting Information).

Interestingly, when optimally doped, DCF3Cz-IPN films showed a fluorescence band with a full width at half maximum (FWHM) of 73 nm, which is narrower compared to the analogous DPEPO films (FWHM = 84 nm), suggesting more orderly

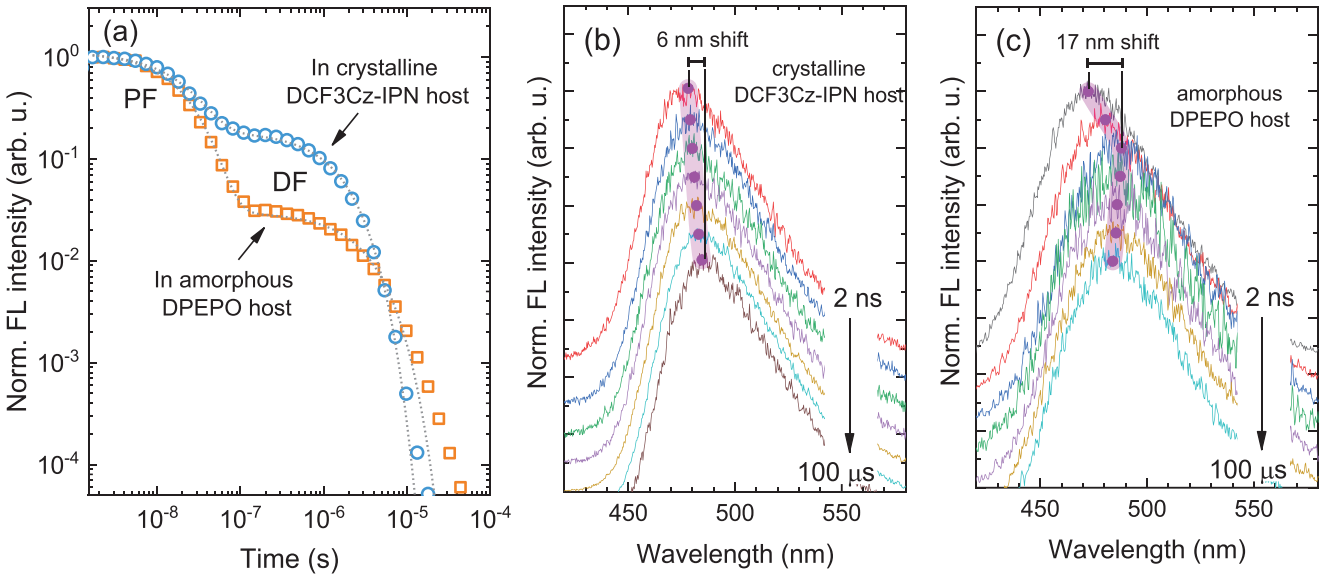

Figure 4. a) Room-temperature FL transients and time-resolved fluorescence spectra of DMeCz-IPN doped b) into DCF3Cz-IPN and c) into DPEPO hosts at 10 wt.% concentration. Dashed lines indicate double-exponential decay fits. Filled circles denote the peak positions of the spectra. Temporal spectral shifts indicated.

arrangement of the dopant DMeCz-IPN molecules (see Figure S9, Supporting Information for the comparison of FL spectra). The reduced disorder was further substantiated by fluorescence transient data (refer to **Figure** 4a), as well as by nearly invariant time-resolved fluorescence spectra (Figure 4b). Both the PF and DF decay components of the doped DCF3Cz-IPN film were nicely fitted by exponential decay models. In contrast, analogous DPEPO film displayed extended DF tails, typically indicative of variation in molecular geometry. This is often associated with a conformational disorder of TADF compounds in the solid state, leading to a temporal red and blue spectral shift of the PF and DF components, respectively.[32,33] In our case, we observed a vast spectral shift of 17 nm in the disordered DPEPO film (Figure 4c). Moreover, a remarkable increase in the DF signal for the doped DCF3Cz-IPN film was obtained, which was caused by an improved Φ_{DF}/Φ_{PF} ratio of 14.6, compared to 4.79 in the DPEPO film (Table 1). The increase was accompanied by a significant shortening of τ_{DF} in the DCF3Cz-IPN film, from 5.26 to 1.52 µs.

The rapid DF was clearly influenced by an impressive boost in k_{RISC}, reaching up to 1.32×10^7 s^{-1}. Meanwhile, the increased DF/PF ratio was determined by a somewhat reduced radiative decay rate ($k_r = 2.39\times10^6$ s^{-1}). Analysis of the low-temperature fluorescence and phosphorescence spectra (Figure S10, Supporting Information) revealed that ΔE_{ST} of DMeCz-IPN is reduced to 20 meV when doped into DCF3Cz-IPN host, which could be the reason for such a drastic increase in k_{RISC}.

To verify the significant changes in ΔE_{ST} upon doping into the DCF3Cz-IPN host, the temperature dependence of FL transients for DMeCz-IPN in different hosts were measured (**Figure** 5a,b). For the DMeCz-IPN compound embedded in the DPEPO matrix a considerable decrease in the DF signal with lowering the temperature was observed. In comparison, the DF signal of the doped DCF3Cz-IPN film expressed significantly less temperature dependence. In fact, a large fraction of DF was still observable even at 60 K. By examining the Arrhenius plots of k_{RISC} (Figure 5c), the RISC activation energies (E_a) for both types of host films were deduced. The disordered DPEPO film had an E_a of 62 meV, which was significantly reduced to 23 meV in the more ordered DCF3Cz-IPN film. This result is in good agreement with the determined ΔE_{ST} values from Figure S10 (Supporting Information) and provides a clear explanation for the observed differences in k_{RISC}.

In order to elucidate the origin of the boosted RISC and reduced E_a of DMeCz-IPN when doped into the DCF3Cz-IPN host, the film morphology was probed. Scanning electron microscopy (SEM) studies revealed the crystalline nature of both the neat and doped DCF3Cz-IPN films (**Figure** 6a,b). These films were composed of well-defined crystallites, with sizes up to several hundred nanometers. Conversely, the neat DMeCz-IPN (Figure 6c) and doped DPEPO (Figure 6d) films were found to be highly homogeneous, implying an amorphous film morphology. The strong likelihood of DCF3Cz-IPN film crystallization was supported by the absence of a glass transition temperature (T_g) and a high melting point temperature (T_m = 362 °C), as obtained from differential scanning calorimetry (DSC) measurements (see Figure S11, Supporting Information). Thus, considering the efficient host-to-dopant FRET and the exponential fluorescence transients discussed earlier, it is reasonable to assume that the solution-grown DCF3Cz-IPN crystallites are uniformly doped with DMeCz-IPN molecules. Furthermore, SEM analysis of the doped crystalline films annealed at temperatures ranging from 100 to 250 °C revealed no significant morphological changes up to 150 °C, indicating their potential suitability for applications in OLEDs (see Figure S12, Supporting Information and explanation therein).

Millimetre-sized single crystals of doped and pure DCF3Cz-IPN were intentionally grown to study the molecular packing and geometries by X-ray diffraction (XRD) measurements. The

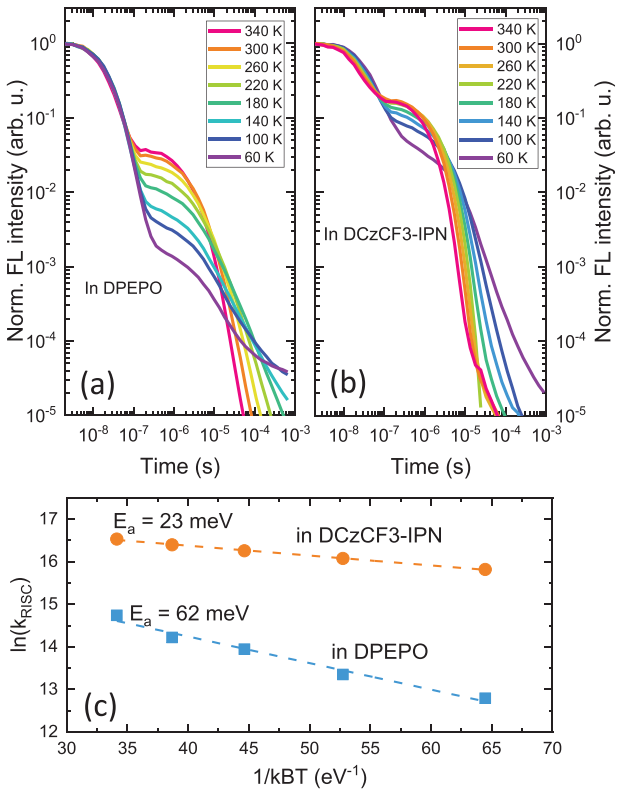

Figure 5. Log-log plots of FL transients of DMeCz-IPN in a) DPEPO and b) DCF3Cz-IPN hosts at 10 wt.% doping concentration as a function of temperature. c) Arrhenius plots of k_{RISC} of the studied doped films.

pure DCF3Cz-IPN crystals were found to be less emissive compared to the highly fluorescent doped ones (**Figure** 7a,b), which were grown from a mixture of DCF3Cz-IPN and DMeCz-IPN in a 10:1 ratio. The XRD analysis revealed that the DCF3Cz-IPN crystals adopt the triclinic crystal system (P-1 space group) with the following lattice parameters: a = 11.0072(5) Å, b = 11.3816(4) Å, c = 12.3108(4) Å, α = 73.252(3)°, β = 80.446(3)°, γ = 68.212(4)°, V = 1368.34(10) Å^3. Each unit cell comprises two molecules (Z = 2) with a single molecule in the asymmetric unit (Z' = 1). Figure 7c,d beautifully illustrates the molecular geometry and packing arrangement, respectively, while the detailed crystallographic data for both doped and pure crystals is provided in Table S3 (Supporting Information). XRD-derived single crystal structure of pure DMeCz-IPN, featuring dihedral angles of 73° and 62° between Cz donors and IPN acceptor, was published elsewhere.[23] In contrast, the Cz planes of DCF3Cz-IPN were determined to form larger angles of 85° and 86° with the IPN acceptor, which is in good agreement with DFT calculations. Importantly, the doped crystals, grown from the mixture of DCF3Cz-IPN and DMeCz-IPN belonged to the same P-1 space group and possessed nearly identical unit cell parameters: a = 11.0542(3) Å, b = 11.3398(4) Å, c = 12.2756(3) Å, α = 73.054(2)°, β = 80.318(2)°, γ = 68.322(3)°, V = 1364.68(8) Å^3. Although the host DCF3Cz-IPN molecules maintained their geometry, the best-fitting parameters were achieved when the crystallographic occupancy of fluorine atoms was set to 0.9. This aligns with the fact that 10% of the total crystal molecules contain –CH_3 moieties instead of –CF_3. Surprisingly, no additional charge density peaks were observed, indicating that DMeCz-IPN adopts the geometry and structural arrangement of the surrounding DCF3Cz-IPN molecules, leading to a more twisted D-A configuration that is expected to alleviate ΔE_{ST}. These structural modifications experienced by DMeCz-IPN upon incorporation into crystalline DCF3Cz-IPN host evidently account for the reduced E_a and the boost of k_{RISC} to beyond 10^7 s^{-1}.

Since the k_{RISC} is also governed by the squared matrix element of the SOC, $|\langle S_1|\hat{H}_{SOC}|T_n\rangle|^2$, where $\hat{H}_{SOC}$ is the spin-orbit coupling operator, the SOC was calculated for the different geometries adopted by DMeCz-IPN in the amorphous DPEPO and crystalline DCF3Cz-IPN hosts. In the case of the amorphous host, the DFT-optimized geometry of the relaxed triplet state of DMeCz-IPN dopant was employed, whereas the XRD-derived DMeCz-IPN geometry was used for the crystalline DCF3Cz-IPN medium. The SOC matrix elements were obtained for the two close-lying transitions, T_1, $T_2 \rightarrow S_1$, under both geometries (Table S4, Supporting Information). In both hosts, the maximum values of the matrix elements were found to be 0.71 and 0.97 cm^{-1}, suggesting that the small differences in their values cannot account for the one-order-of-magnitude differences in k_{RISC} between the two hosts. We note that the reduced reorganization energy in the case of the crystalline host may also contribute to the enhanced k_{RISC}.[34] However, the exact contribution remains elusive due to the inherent difficulties in assessing changes in the excited state molecular geometry within the crystalline environment.

The demonstrated concept of molecular geometry adaptation to crystalline host represents a novel approach to host-driven RISC engineering of emitting TADF dopants. This approach offers several distinct advantages: i) by locking the D-A twist angles, it suppresses conformational disorder and emission wavelength variation, resulting in a narrower emission bandwidth; ii) it remarkably bolsters k_{RISC}, thereby reducing triplet population and fatal triplet-mediated annihilation events; and iii) it shortens the delayed fluorescence lifetime, further promoting TADF process. While currently seeming impractical, blue TADF-OLEDs based on such smartly designed crystalline host-guest emissive layers hold the potential of dramatically diminishing triplet-mediated annihilation effects, the primary cause of device efficiency roll-off and premature degradation. Furthermore, from a materials perspective, crystalline emissive layers with enhanced morphological stability should be capable of tolerating higher current densities, making them promising candidates for high-performance, long-lasting blue OLEDs.

3. Conclusion

In summary, a novel approach to enhance the performance of TADF emitters via the manipulation of RISC using crystalline host-driven engineering is introduced. The approach enables the boosting of RISC for TADF emitters upon doping into a crystalline host through the molecular geometry adaption of the emitter to that of the host. This strategy aims to address the challenges of blue TADF-OLEDs associated with severe efficiency roll-off and poor device stability.

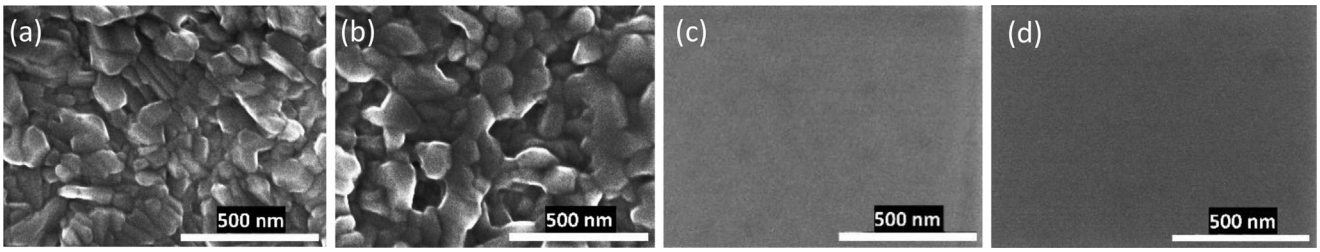

Figure 6. SEM images of a) the neat DCF3Cz-IPN film, b) the DCF3Cz-IPN film doped with 10 wt.% DMeCz-IPN, c) the neat DMeCz-IPN film, d) DPEPO film doped with 10 wt.% DMeCz-IPN.

The approach was validated using the designed host-guest system comprising the efficient blue TADF emitter 4,6-bis(1-methylcarbazol-9-yl)benzene-1,3-dicarbonitrile (DMeCz-IPN) as a guest and a crystalline host 4,6-bis[1-(trifluoromethyl)carbazol-9-yl]benzene-1,3-dicarbonitrile (DCF3Cz-IPN). The host, with a molecular structure identical to the dopant except for the inclusion of more sterically demanding trifluoromethyl (-CF3) groups, displayed a more twisted (nearly orthogonal) D-A geometry. As confirmed by XRD studies, the realization of doped crystals has been found to induce changes in the geometry of the dopant, aligning it with the more twisted structural configuration of the host. The geometry modifications were found to reduce ΔE_{ST}, leading to an impressive almost tenfold boost in the RISC rate (up to 1.32×10^{7} s^{-1}) and a substantial fourfold reduction in the delayed FL lifetime (down to 1.52 µs), as evidenced by delayed FL and quantum yield measurements.

Furthermore, in contrast to the amorphous host, the ordered molecular arrangement in the crystalline host suppressed conformational disorder and emission wavelength variation, resulting in a narrower emission bandwidth and, consequently, improved color purity. This is crucial for the blue TADF-OLEDs, as the emission bandwidth directly impacts the color purity. While currently impractical, blue TADF-OLEDs based on crystalline emissive layers with enhanced morphological stability should be capable of tolerating higher current densities, making them promising candidates for high-efficiency, stable blue OLEDs.

4. Experimental Section

Amorphous DPEPO films doped with 10 wt.% of the IPN compounds were prepared by spin-coating chloroform solutions (10 mg mL^{-1}) of DPEPO and IPN mixtures onto quartz substrates at 2000 rpm. In contrast, crystalline DCF3Cz-IPN films (neat and doped) as well as amorphous DMeCz-IPN films were spin-coated using the same concentration and spin-coating parameters, but with THF as the solvent. Both amorphous and crystalline films were subsequently annealed at 100 °C for 5 min to remove residual solvent. Absorption spectra of the investigated compounds in toluene solutions (10^{-5} M) were measured using a UV–vis–NIR spectrophotometer Lambda 950 (Perkin Elmer). The absorption

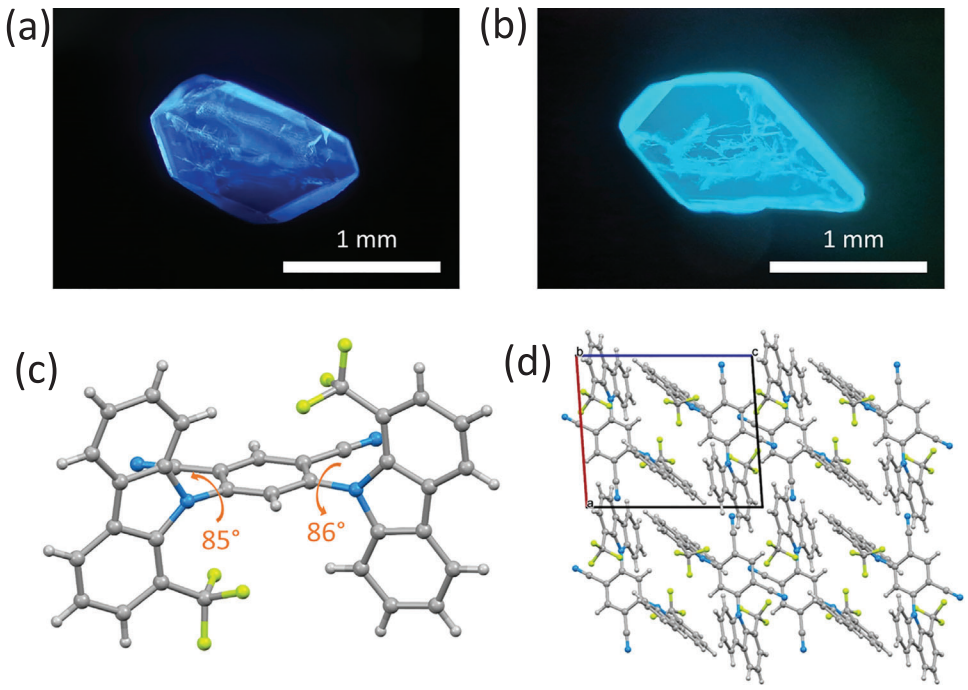

Figure 7. Fluorescence microscopy images of a) pure and b) 10 wt.% DMeCz-IPN doped DCF3Cz-IPN single crystals. c) Molecular geometry and d) molecular packing of DCF3Cz-IPN in a single crystal.

properties of the films were assessed by measuring excitation spectra using FLS980 spectrometer (Edinburgh Instruments). Back-thinned CCD spectrometer PMA-12 (Hamamatsu) was employed to measure steady-state fluorescence (FL) spectra by exciting samples with a xenon lamp coupled to a monochromator. FL quantum yields (Φ_{FL}) of the films were estimated by employing integrating sphere (Sphere Optics). FL transients and time-resolved photoluminescence spectra were obtained using nanosecond YAG:Nd^{3+} laser NT 242 equipped with an optical parametric oscillator (Ekspla, excitation wavelength 340 nm, pulse duration 5 ns, repetition rate 1 kHz) and time-gated intensified CCD camera iStar DH340T (Andor) mounted on a spectrograph SR-303i (Shamrock). Low-temperature measurements were carried out in a closed-cycle helium cryostat 204N (Cryo Industries of America).

Optimization of ground state geometries was carried out in toluene by employing density functional theory (DFT) with revPBE38 functional at 6–31G(d) basis, implemented in ORCA 5.0 software.[35] Time-dependent DFT (TD-DFT) method, at the same basis set level, was used for the evaluation of transition energies (*E*) from ground to excited state, oscillator strengths (*f*), as well as the highest occupied (HOMO) and lowest unoccupied (LUMO) molecular orbitals.

Cyclic voltammetry (CV) measurements were conducted in a three-electrode cell. A Pt/Ti wire was used as the counter-electrode, an Ag/AgCl electrode served as the reference electrode, and a glassy-carbon electrode functioned as the working electrode.

Single crystals for XRD analysis were grown by the diffusion of diethyl ether vapor into chloroform solutions. Suitable crystals were selected and analyzed on an XtaLab Synergy diffractometer (Rigaku), equipped with a HyPix-6000HE hybrid photon counting detector and a PhotonJet microfocus X-ray source (CuKα, $\lambda = 1.54184$). Data were collected and processed using the CrysAlisPro software. The structures were solved by Intrinsic Phasing with the ShelXT[36] program and refined with the ShelXL[37] package, using Least Squares minimization and employing the Olex2 graphical interface.[38] The structure file of the DCF3Cz-IPN crystal was deposited with the Cambridge Crystallographic Data Centre and is available free of charge (CCDC 2 308 707).

Fluorescence microscope BX51 (Olympus) was used to obtain images of single crystals. The morphology of the films was investigated with an SU8230 scanning electron microscope (Hitachi). The films for these measurements were prepared by spin-coating on glass/ITO substrates.

All materials and reagents were purchased from available commercial suppliers unless stated otherwise.

Supporting Information

Supporting Information is available from the Wiley Online Library or from the author.

Acknowledgements

The research was funded by a grant (no. S-MIP-21-12) from the Research Council of Lithuania (LMTLT). T.J. and E.O. acknowledge the "Universities' Excellence Initiative" programme by the Ministry of Education, Science and Sports of the Republic of Lithuania under the agreement with the Research Council of Lithuania (project No. S-A-UEI-23-6).

Conflict of Interest

The authors declare no conflict of interest.

Data Availability Statement

The data that support the findings of this study are available in the supplementary material of this article.

Keywords

crystalline TADF, isophthalonitrile, reverse intersystem crossing, RISC manipulation

Received: January 3, 2024
Revised: February 26, 2024
Published online: March 14, 2024

[1] J. Bauri, R. B. Choudhary, G. Mandal, *J. Mater. Sci.* **2021**, *56*, 18837.
[2] H. A. Skinner, J. A. Connor, *Pure Appl. Chem.* **1985**, *57*, 79.
[3] J. Sun, H. Ahn, S. Kang, S. B. Ko, D. Song, H. A. Um, S. Kim, Y. Lee, P. Jeon, S. H. Hwang, Y. You, C. Chu, S. Kim, *Nat. Photonics* **2022**, *16*, 212.
[4] H. Uoyama, K. Goushi, K. Shizu, H. Nomura, C. Adachi, *Nature* **2012**, *492*, 234.
[5] H. Lim, H. J. Cheon, S. J. Woo, S. K. Kwon, Y. H. Kim, J. J. Kim, *Adv. Mater.* **2020**, *32*, 2004083.
[6] S. Hirata, Y. Sakai, K. Masui, H. Tanaka, S. Y. Lee, H. Nomura, N. Nakamura, M. Yasumatsu, H. Nakanotani, Q. Zhang, K. Shizu, H. Miyazaki, C. Adachi, *Nat. Mater.* **2015**, *14*, 330.
[7] J. W. Sun, J. H. Lee, C. K. Moon, K. H. Kim, H. Shin, J. J. Kim, *Adv. Mater.* **2014**, *26*, 5684.
[8] B. van der Zee, Y. Li, G. J. A. H. Wetzelaer, P. W. M. Blom, *Adv. Opt. Mater.* **2021**, *9*, 2100249.
[9] S. K. Jeon, H. L. Lee, K. S. Yook, J. Y. Lee, *Adv. Mater.* **2019**, *31*, 1803524.
[10] J. Jiang, J. Y. Lee, *Mater. Today* **2023**, *68*, 204.
[11] Q. Zhang, B. Li, S. Huang, H. Nomura, H. Tanaka, C. Adachi, *Nat. Photonics* **2014**, *8*, 326.
[12] C. Murawski, K. Leo, M. C. Gather, *Adv. Mater.* **2013**, *25*, 6801.
[13] D. Banevičius, G. Kreiza, R. Kliooštoraitis, S. Juršėnas, T. Javorskis, V. Vaitkevičius, E. Orentas, K. Kazlauskas, *J. Mater. Chem. C* **2021**, *10*, 4813.
[14] C. H. Ryoo, J. Han, J. hoon Yang, K. Yang, I. Cho, S. Jung, S. Kim, H. Jeong, C. Lee, J. E. Kwon, I. E. Serdiuk, S. Y. Park, *Adv. Opt. Mater.* **2022**, *10*, 2201622.
[15] G. Kreiza, D. Banevičius, J. Jovaišaitė, S. Juršėnas, T. Javorskis, V. Vaitkevičius, E. Orentas, K. Kazlauskas, *J. Mater. Chem. C* **2020**, *8*, 8560.
[16] P. K. Samanta, D. Kim, V. Coropceanu, J. L. Brédas, *J. Am. Chem. Soc.* **2017**, *139*, 4042.
[17] Z. Zhao, S. Yan, Z. Ren, *Acc. Chem. Res.* **2023**, *56*, 1942.
[18] M. Saigo, K. Miyata, S. Tanaka, H. Nakanotani, C. Adachi, K. Onda, *J. Phys. Chem. Lett.* **2019**, *10*, 2475.
[19] B. Li, Z. Li, X. Wei, F. Guo, Y. Wang, L. Zhao, Y. Zhang, *J. Mater. Chem. C* **2019**, *7*, 9966.
[20] Y. H. Lee, Y. S. Shin, T. Lee, J. Jung, J. H. Lee, M. H. Lee, *Chem. Eng. J.* **2021**, *423*, 130224.
[21] H. J. Cheon, S. J. Woo, S. H. Baek, J. H. Lee, Y. H. Kim, *Adv. Mater.* **2022**, *34*, 2207416.
[22] H. Noda, H. Nakanotani, C. Adachi, *Sci. Adv.* **2018**, *4*, aao6910.
[23] G. Kreiza, D. Berenis, D. Banevičius, S. Juršėnas, T. Javorskis, E. Orentas, K. Kazlauskas, *Chem. Eng. J.* **2021**, *412*, 128574.
[24] H. Yersin, R. Czerwieniec, L. Mataranga-Popa, J. M. Mewes, G. Cheng, C. M. Che, M. Saigo, S. Kimura, K. Miyata, K. Onda, *Adv. Funct. Mater.* **2022**, *32*, 2201772.
[25] P. L. Dos Santos, J. S. Ward, M. R. Bryce, A. P. Monkman, *J. Phys. Chem. Lett.* **2016**, *7*, 3341.
[26] J. Yang, D. Hu, F. Zhu, Y. Ma, D. Yan, *Sci. Adv.* **2022**, *8*, add1757.
[27] X. Yang, X. Feng, J. Xin, P. Zhang, H. Wang, D. Yan, *J. Mater. Chem. C* **2018**, *6*, 8879.

[28] N. Della Ca', G. Sassi, M. Catellani, *Adv. Synth. Catal.* **2008**, *350*, 2179.
[29] C. Chen, Z. Chi, K. C. Chong, A. S. Batsanov, Z. Yang, Z. Mao, Z. Yang, B. Liu, *Nat. Mater.* **2020**, *20*, 175.
[30] N. Aizawa, A. Matsumoto, T. Yasuda, *Sci. Adv.* **2021**, *7*, 5769.
[31] G. Kreiza, D. Banevičius, J. Jovaišaitė, K. Maleckaitė, D. Gudeika, D. Volyniuk, J. V. Gražulevičius, S. Juršėnas, K. Kazlauskas, *J. Mater. Chem. C* **2019**, *7*, 11522.
[32] T. Serevičius, R. Skaisgiris, J. Dodonova, K. Kazlauskas, S. Juršėnas, S. Tumkevičius, *Phys. Chem. Chem. Phys.* **2019**, *22*, 265.
[33] T. Serevičius, R. Skaisgiris, I. Fiodorova, G. Kreiza, D. Banevičius, K. Kazlauskas, S. Tumkevičius, S. Juršėnas, *J. Mater. Chem. C* **2021**, *9*, 836.
[34] I. E. Serdiuk, M. Monka, K. Kozakiewicz, B. Liberek, P. Bojarski, S. Y. Park, *J. Phys. Chem. B* **2021**, *125*, 2696.
[35] F. Neese, *Wiley Interdiscip. Rev. Comput. Mol. Sci.* **2022**, *12*, e1606.
[36] G. M. Sheldrick, *Acta Crystallogr. Sect. A Found. Crystallogr.* **2015**, *71*, 3.
[37] G. M. Sheldrick, *Acta Crystallogr. Sect. C Struct. Chem.* **2015**, *71*, 3.
[38] O. V. Dolomanov, L. J. Bourhis, R. J. Gildea, J. A. K. Howard, H. Puschmann, *J. Appl. Crystallogr.* **2009**, *42*, 339.